3D Structured Optical Fiber Pressure Sensors

Tongyu Liu, Zipei Song, Richard J. Reeves, Mohan Wang, Crispin T.M. Doyle, Martin J. Booth, and Julian A.J. Fells

***Abstract*—Pressure sensors based on fiber Bragg gratings in side-hole optical fiber enable remote monitoring of pressure at multiple points within many otherwise inaccessible environments. However, sensors fabricated from side-hole fiber drawn from a preform have limitations in their design and material composition. The design of such sensors is a compromise between achieving good sensitivity, while also minimizing splice losses due to mode-mismatch. We have developed optimized designs for pressure sensors with complex 3D structures using simulations and fabricated them within commercial step-index fibers. The fabrication uses a femtosecond laser in conjunction with selective etching to write precisely defined voids within the fiber cladding. The sensors were tested in a hydraulic system up to 600 bar and achieved a sensitivity of 0.41 pm/bar. The technique has potential for enabling pressure sensors in many types of high-performance fibers for a range of sensing applications.**

***Index Terms*—Pressure sensors, Fiber Bragg Grating, Femtosecond Laser, birefringence.**

I. Introduction

PRESSURE sensors are needed for monitoring a wide range of infrastructure for performance and safety. Compared to traditional electronic sensors, optical fiber sensors are immune to electromagnetic interference and able to operate in explosive environments [1]. Many applications, such as space, biomedicine and aerospace are very sensitive to mass and size, and optical fiber sensors have very significant advantages over traditional electronic sensors in this respect [2]. Furthermore, there is a desire to extend pressure monitoring into ultra-extreme environments such as gas turbines and nuclear reactors, beyond the capabilities of silica fiber.

Fabry-Pérot sensors have been used for pressure sensing, but these are unsuitable for multiplexing multiple sensors on a single fiber [3]. An alternative solution is to use optical fiber drawn with air holes in the cladding along the length of the fiber [4], [5]. When exposed to external pressure, there is a stress induced birefringence, which can be detected with polarimetry. Fiber Bragg gratings (FBGs) may be incorporated into this fiber for high sensitivity pressure measurements at specific points. These sensors have two Bragg reflection peaks and their wavelength separation is a measure of pressure, while their absolute wavelengths can be used to determine temperature [4], [6]. An inherent advantage of air-hole fiber pressure sensors is that they give independent measurements of pressure and temperature simultaneously with a single sensor. This avoids the need to have additional sensors in order to correct for the effect of temperature which is often required for FBG sensors [7], [8]. The sensitivity has been further improved using a microstructure air-hole fiber [9]. However, there are limitations in the design of air-hole fibers drawn from preforms, which put restrictions on the size of the holes, their shape and their placement within the fiber. There is also a mode mismatch between these speciality fibers and standard single mode fiber, resulting in high splice losses, which can severely restrict the number of concatenated sensors. For example, the round trip splice loss in Ref. [9] was 12 dB.

In this paper, we design and fabricate three-dimensional custom holes in step-index fiber to allow high sensitivity without incurring large splice losses. The technique also has the potential for use in exotic fibers for extreme environments.

II. Sensor Principle

From the Bragg equation (1), it is found that when the effective refractive index of the mode, n_{eff}, or the grating pitch, Λ, changes, the reflective center wavelength changes in response.

$$\lambda_B = 2n_{neff}\Lambda \tag{1}$$

Sensors based on air-hole fiber are able to measure pressure and temperature independently. Incorporating air holes into an optical fiber results in an uneven stress distribution inside the fiber when subjected to external pressure. This in turn will cause the refractive index of the fiber to become anisotropic via the stress-optic effect [10], [11],

$$\Delta B_{ij} = P_{ijkl}S_{kl} \tag{2}$$

where $B_{ij} = (1/n^2)_{ij}$, ΔB_{ij} is inverse permittivity tensor, P_{ijkl} is fourth order stress-optic tensor and S_{kl} is second order strain tensor. The radial vector length of the refractive index ellipsoid represents the index component in the direction of the light vibration. It needs to satisfy the following conditions,

$$\begin{gathered} B_{ij} = X_i X_j = 1 \\ [B_{ij}(0)+\Delta B_{ij}]X_i X_j = 1 \end{gathered} \tag{3}$$

Manuscript received 15 March 2024; revised 30 July 2024; accepted 31 July 2024. Date of publication xxxxxxx; date of current version xxxxxxx. This work was supported by the U.K. Engineering and Physical Sciences Research Council under Grant EP/T00326X/1. (Corresponding author: Julian A.J. Fells).

Tongyu Liu, Zipei Song, Richard J. Reeves, Mohan Wang, Martin J. Booth, and Julian A.J. Fells are with the Department of Engineering Science, University of Oxford, Parks Road, Oxford OX1 3PJ, UK. (e-mail: tongyu.liu@eng.ox.ac.uk; zipei.song@eng.ox.ac.uk; richard.reeves@eng.ox.ac.uk; mohan.wang@eng.ox.ac.uk; martin.booth@eng.ox.ac.uk; julian.fells@eng.ox.ac.uk). Crispin T.M. Doyle is with Halliburton, Spectrum House, Brants Bridge, Bracknell RG12 9BG, UK. (e-mail: crispin.doyle@halliburton.com).

Color versions of one or more figures in this article are available at xxxxxxxx. Digital Object Identifier xxxxxxxx

Considering that ΔB_{ij} and S_{kl} are symmetric tensors, the number of independent parameters in equation (2) can be reduced. Expanding equation (2) gives the following form,

$$\begin{bmatrix}\Delta B_1\\ \Delta B_2\\ \Delta B_3\\ \Delta B_4\\ \Delta B_5\\ \Delta B_6\end{bmatrix} = \begin{bmatrix}P_{11} & P_{12} & P_{13} & P_{14} & P_{15} & P_{16}\\ P_{21} & P_{22} & P_{23} & P_{24} & P_{25} & P_{26}\\ P_{31} & P_{32} & P_{33} & P_{34} & P_{35} & P_{36}\\ P_{41} & P_{42} & P_{43} & P_{44} & P_{45} & P_{46}\\ P_{51} & P_{52} & P_{53} & P_{54} & P_{55} & P_{56}\\ P_{61} & P_{62} & P_{63} & P_{64} & P_{65} & P_{66}\end{bmatrix}\begin{bmatrix}\varepsilon_x\\ \varepsilon_y\\ \varepsilon_z\\ 2\tau_{yz}\\ 2\tau_{xz}\\ 2\tau_{xy}\end{bmatrix} \tag{4}$$

Also since the material of the fiber is silica, we can assume the material is isotropic when no pressure is applied, which gives us the following equation,

$$\begin{bmatrix}\Delta B_1\\ \Delta B_2\\ \Delta B_3\\ \Delta B_4\\ \Delta B_5\\ \Delta B_6\end{bmatrix} = \begin{bmatrix}P_{11} & P_{12} & P_{12} & 0 & 0 & 0\\ P_{12} & P_{11} & P_{12} & 0 & 0 & 0\\ P_{12} & P_{12} & P_{11} & 0 & 0 & 0\\ 0 & 0 & 0 & m & 0 & 0\\ 0 & 0 & 0 & 0 & m & 0\\ 0 & 0 & 0 & 0 & 0 & m\end{bmatrix}\begin{bmatrix}\varepsilon_x\\ \varepsilon_y\\ \varepsilon_z\\ 0\\ 0\\ 0\end{bmatrix} \tag{5}$$

The relation between the stress and the induced refractive index change can be described by,

$$\begin{aligned} n_1 &= n_0 - 0.5n_0^3(P_{11}\varepsilon_x + P_{12}\varepsilon_y + P_{12}\varepsilon_z)\\ n_2 &= n_0 - 0.5n_0^3(P_{12}\varepsilon_x + P_{11}\varepsilon_y + P_{12}\varepsilon_z)\\ n_3 &= n_0 - 0.5n_0^3(P_{12}\varepsilon_x + P_{12}\varepsilon_y + P_{11}\varepsilon_z)\end{aligned} \tag{6}$$

where P_{11}, P_{12} are the stress-optic coefficients, ϵ_x, ϵ_y, ϵ_z are the stress components, n_1, n_2, n_3 are the refractive index components and n_o is the unstressed refractive index. This anisotropy will change the effective refractive index of each orthogonal polarization mode differently. According to the Bragg equation, the central reflection wavelength of the FBG will shift as the effective refractive index changes. Hence, since the orthogonal polarization modes have different effective indices, they will also have different Bragg wavelengths. This will result in a splitting of the reflection peak if light is launched into both polarizations. In contrast, although the refractive index will also change with temperature, this change is isotropic and will not alter the wavelength separation between the two peaks.

III. Device Simulation and Optimization

To model and optimize the structure of the sensor, we used the multi-physics field simulation software COMSOL to calculate the distribution of internal stresses in the fiber when it is exposed to external pressure. Then we calculated the refractive index distribution by bringing the results of the stress distribution into the stress-optic equation. We simulate the FBG in the modified fiber based on these data and calculate its transmission peak. We then obtain the response of the sensor under external pressure changes. We investigated sensors in both standard single-mode fiber (SMF) and large cladding fiber (LCF) with diameters of 220 μm and 250 μm.

The starting point for the design is a bow-tie hole structure, in order to obtain higher sensitivity than conventional circular holes. The bow-tie consists of two sectors filled with air.

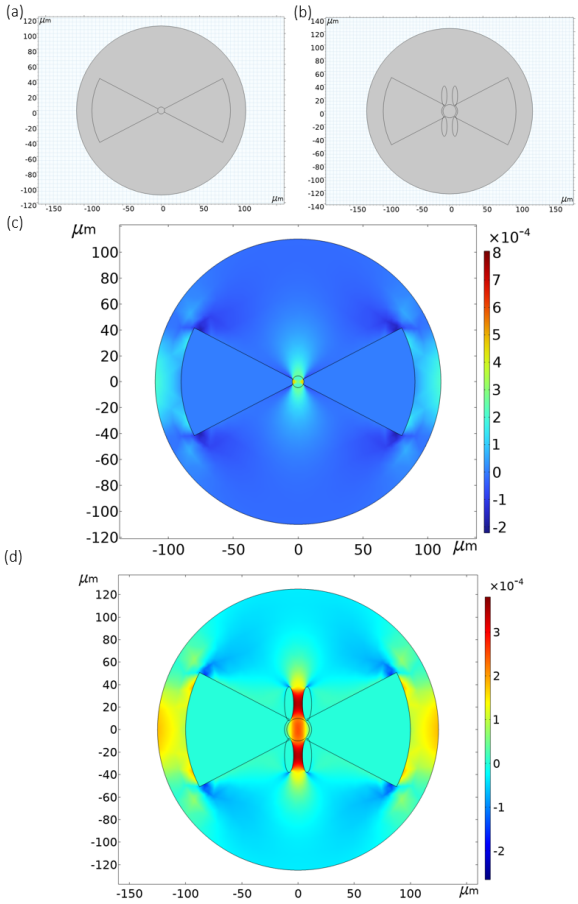


Fig. 1. Simulation results of the distribution of the change in refractive index components over different fiber cross-sections when an external 124 bar pressure is applied. (a) Layout of sector holes in a 220 μm diameter fiber, (b) layout of sector holes with micro-holes in a 250 μm diameter fiber, (c) simulation of sector holes, (d) simulation of sector holes with micro-holes.

Figure 1(a) shows the layout of the holes and Fig. 1(c) shows simulation results of the change in refractive index when an external 124 bar pressure is applied. Different shapes and sizes of air holes can have a significant effect on the sensitivity of the sensor. To further improve sensitivity, adding additional micro-holes around the fiber core was also investigated, as shown in Figure 1(b). The simulation results of the change in refractive index of this structure are shown in Fig. 1(d) when an external 124 bar pressure is applied.

In order to calculate the Bragg reflection peaks for the two orthogonal polarization modes, the refractive index data was imported into FIMMWAVE (Photon Design Limited). This was used to generate simulated spectra for the two polarization modes. We explored the parameter space by first varying the sector angle. We set the radius of the sector to 90 μm and performed a parameter sweep for the sector angle, which ranged from 40° to 90°. If the angle is too large the hollow area will also become too large and the sensor structure will be unstable. The results in Fig. 2 show the maximum transmission peak separation is 0.3 nm for a sector angle of 55 degrees at an external pressure of 124 bar. After optimising the sector angle, the simulation results also show that adding micro-holes near

the core can improve the sensitivity more efficiently than just optimising the simple geometry, Table 1 shows the sensitivity simulation results for three different designs.

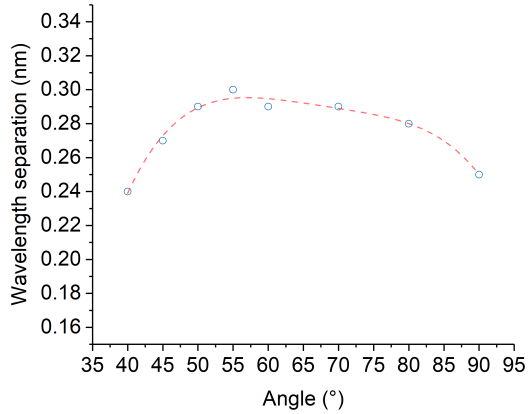


Fig. 2. Parameter sweep for the sector angle for a 220 μm diameter fiber at an external pressure of 124 bar.

TABLE I
SIMULATION RESULTS OF SENSITIVITY IN DIFFERENT TYPES OF OPTICAL FIBER.

Diameter	Type	Sensitivity
125 μm	Sector hole	1.128 pm/bar
220 μm	Sector hole	2.417 pm/bar
250 μm	Sector hole with elliptical micro-holes	3.304 pm/bar

After analysing the influence of the shape of the air holes, it is also important to ensure that the response of the sensor to changes in pressure is linear. Figure 3 shows the simulated

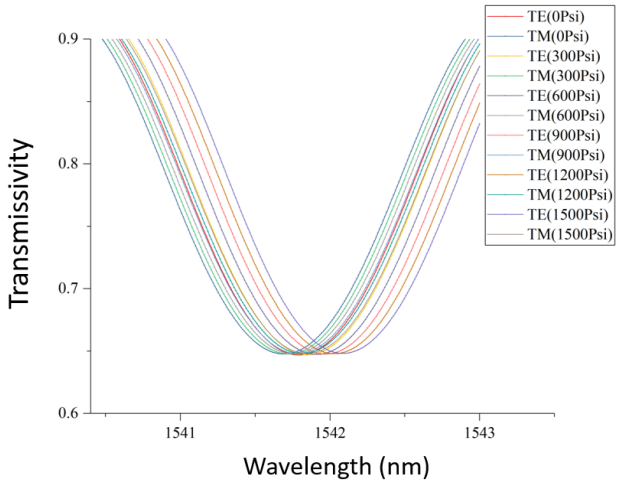


Fig. 3. FBG transmissivity in two polarization directions at different pressure.

transmission spectra of the two polarization modes at different pressures, while at constant temperature. From this data, the peak separation verses pressure is shown in Fig. 4. These results show that the response of the sensor maintains a good degree of linearity. Another key point is to make sure that temperature changes can be decoupled from pressure changes.

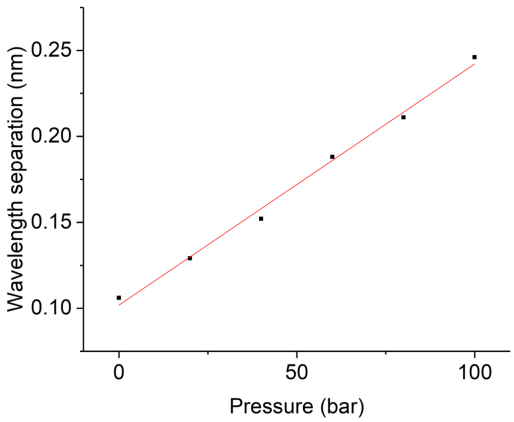


Fig. 4. Relation between wavelength separation and pressure change for a 220 μm diameter fiber.

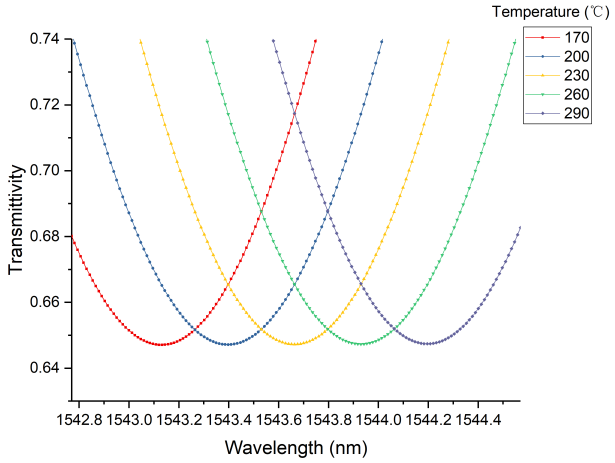


Fig. 5. Simulation results of FBG peak at different temperatures for a 220 μm diameter fiber.

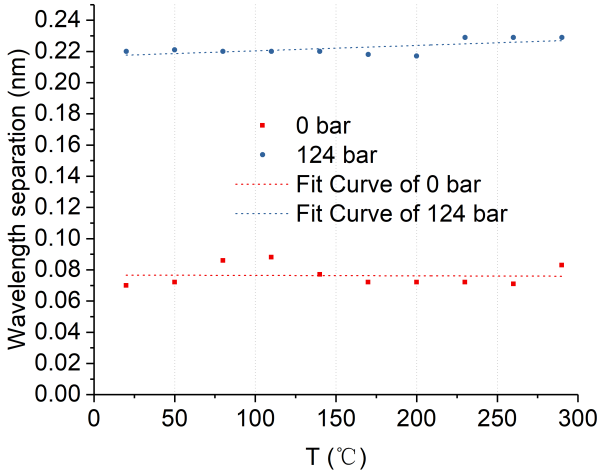


Fig. 6. Simulation of peak separation at different temperatures and pressures for a 220 μm diameter fiber.

We introduced thermal expansion into the model to calculate the transmission spectra at different pressures and temperatures and obtained the simulation results as shown in Fig. 5 and Fig. 6. Figure. 5 shows the effect of varying temperature at constant

pressure, resulting in a shift of the FBG peak. Figure. 6 shows the performance of the sensor as the temperature is varied, for two different constant pressures.

It is clear that at different temperatures, the relative peak separation changes only very slightly and the response is dominated by just an overall translation of both peaks. However, the amount of wavelength separation between the peaks changes consistently at different pressures. These results show that temperature and pressure data can be acquired simultaneously for this type of sensor.

IV. Device Fabrication

Devices were fabricated within both SMF and LCF (LIEKKI® Passive-12/250DC). The fiber was first exposed to a femtosecond laser to write a 6 mm second order FBG (period 1073 nm) by the line-by-line method [12]. The femtosecond laser was then used to define the areas to be removed. When the silica is exposed to the femtosecond laser pulses of appropriate pulse energy, nanogratings are formed. The fibers were then placed in an etchant, which selectively removes the material in these defined areas. The laser used for sample fabrication was a femtosecond laser (Light Conversion, Pharos) operating at 515 nm with a linear polarization and 170 fs pulse duration. An oil immersion objective (Olympus UPlanAPO 20×, NA 0.85) was used to focus the beam within the fiber. The laser power used was in the range of 90 mW to 130 mW. Sensors with sector air-holes were fabricated in the SMF and sensors with sectors and elliptical micro-holes were fabricated in the LCF.

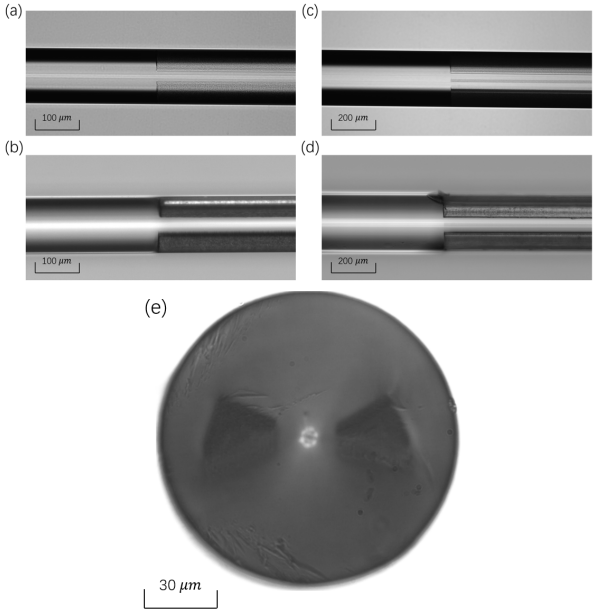


Fig. 7. Microscope image of the samples. (a),(b) Side views of the inscribed and uninscribed areas of the 125 μm SMF before and after etching. (c),(d) Side views of the inscribed and uninscribed areas of the 250 μm large diameter fiber before and after etching. (e) Cross-sectional view of the 125 μm SMF inscription area.

After laser exposure, the fiber was cleaved to expose the inscribed structure. We used 8 mol/L KOH at 85°C for wet etching of the silica fiber because KOH has better selectivity than HF and it is also less hazardous [13], [14]. The microscope images in Fig. 7 demonstrate the accuracy of this selective etching. Although the etched area appears to be through the fiber cladding, this is not the case and it is purely a distortion of the image caused by optical aberrations at the curved silica interface. After the etching is complete, the open air-hole end surface is sealed using a fiber fusion splicer (Fujikura 70R).

V. Device Testing

An LCF sample (95 μm sector radius with micro-holes) was pressure tested using a hydraulic system, shown in Fig. 8. The FBG sensor was was spliced to polyimide coated SMF and placed in a 1/4" internal diameter stainless steel tube. This tube was connected to a T-piece with the fiber end passing through the T-piece onto 1/16" internal diameter stainless-steel tubing which was sealed by epoxy around the fiber. The other end of the tube housing the sensor was connected to the bleed valve, which allows air to be vented from the tube at the beginning of each test, letting the hydraulic oil fill the whole system. A hand-hydraulic pump from Enerpac was connected to the third port of the T-piece to provide the system with pressure up to 600 bar. All tubing and fittings were from Swagelok and rated to 700 bar.

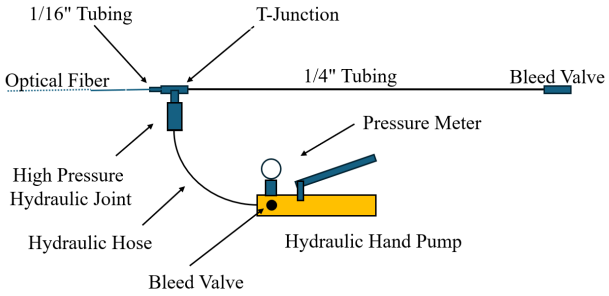


Fig. 8. Hydraulic pressure test systems for FBG sensors

At each pressure, the FBG reflection spectrum was measured by a FBG interrogator (Halliburton SmartFibres SmartScan SBI). Four cycles of pressure tests up to 600 bar in 50 bar steps were made. At each pressure, an averaged spectrum from the interrogator was taken. The standard interrogator configuration has a polarization scrambler to measure the spectra of both polarization modes simultaneously. However, as we had a non-standard configuration without the polarization scrambler, we used a manual polarization controller adjusted to ensure light was launched into both polarization modes. After the first pressure test cycle, a temperature stability test was performed, taking the sample up to 450°C. Figure 9 shows spectra at different pressures for the second test cycle. As the peaks separate their relative power decreases due to the lower overlap. For clarity we have normalized the data to the level of the short-wavelength peak. Below 300 bar, the spectra of the two polarization modes overlap, so it is difficult to discern the pressure. The reflection peak appears to start splitting at 300 bar and the peak

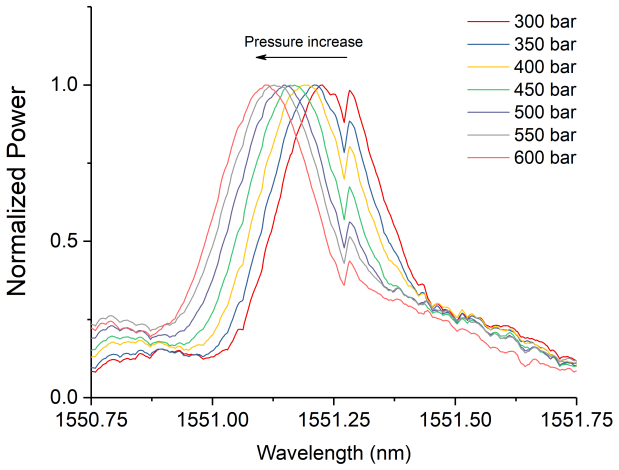


Fig. 9. Normalised pressure test results of the sector holes with elliptical micro-holes sample. See Dataset 1 for the underlying raw data.

separation increases with increasing pressure. At 600 bar the peak separation is approximately 174.4 pm.

A plot of the peak separation versus pressure is provided in Fig. 10, showing a linear relationship for all test cycles. The first test cycle, which was taken before the sample was taken up to 450°C, has a constant offset in the measurement results compared to the other test cycles. However, the three test cycles taken afterwards are all very consistent and repeatable. It appears that taking the temperature up to 450°C has resulted in a thermal annealing. The sensitivity of the sensor does not change after annealing, but the overall peak separation becomes larger, which is due to the fact that annealing releases the thermal stresses introduced by the laser fabrication, which changes the intrinsic birefringence in the optical fiber. From the gradient of the measurements in Fig. 10, the pressure sensitivity is approximately 0.41 pm/bar. The main error in the measurement comes from the low accuracy and stability of the hand hydraulic pump.

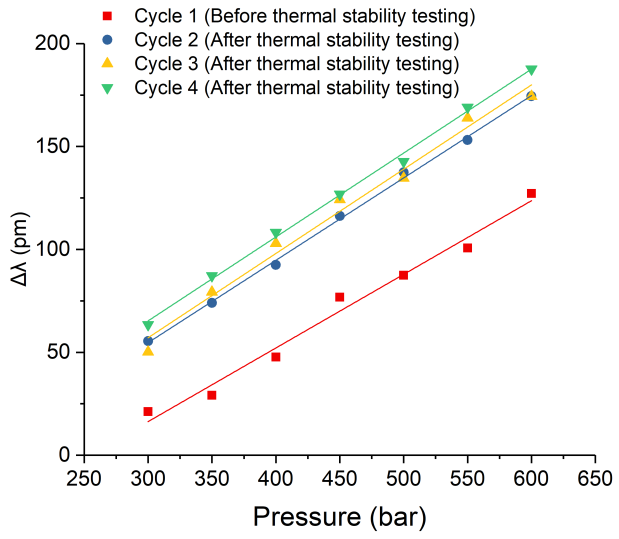


Fig. 10. Pressure test results before and after thermal stability test, with a linear fit. See Dataset 1 for the underlying data.

The results of the thermal stability tests are shown in Fig. 11. The temperature of the sample was taken up to 450°C in 50°C steps at atmospheric pressure. At all temperatures, the reflection peaks of the FBG do not show any sign of separation. This is consistent with our simulation results that the sensor can decouple temperature and pressure. Also the uniform shift of the reflection peaks with temperature demonstrates its potential for measuring both temperature and pressure simultaneously.

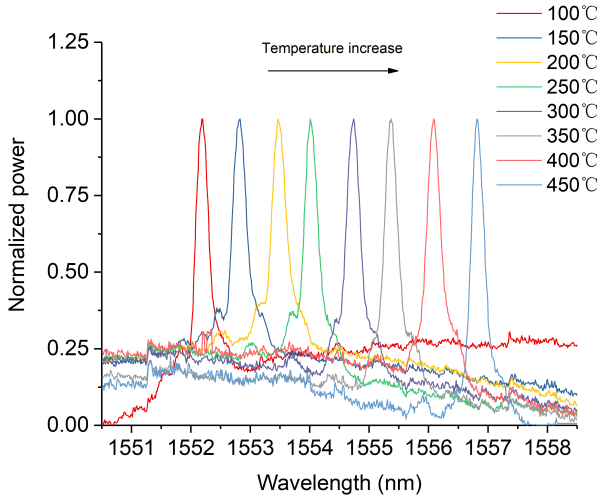


Fig. 11. Thermal stability test results for the sector holes with elliptical micro-holes sample. See Dataset1 for the underlying raw data.

The reason for the difference in sensitivity between the experimental and simulation results is two-fold. Firstly, during fabrication it was necessary to leave a larger distance between the hole and the core to prevent over-etch into the core. This meant that although the sector radius was 95 μm, the radial dimension of the hole was only 83 μm. Secondly, when sealing with the fusion splicer, the optical fiber melting causes the channel to collapse slightly, which results in a smaller-than-expected structural size. The sensitivity could be improved by better process control to allow etching closer to the core and exploring alternative methods for sealing.

The proposed fabrication technique can potentially be applied to many different fibers. Sapphire optical fiber is particularly attractive as it can withstand temperatures up to 2000°C and high radiation. Recently, a single-mode sapphire optical fiber has been demonstrated using femtosecond laser fabrication [15] and sapphire can be etched with very high selectivity using KOH [16]. The new fabrication technique therefore opens up the possibility of optical fiber pressure sensing in ultra-extreme environments.

VI. Conclusions

We demonstrated a new method of pressure sensor fabrication using femtosecond laser writing in conjunction with selective etching to form three dimensional voids in an optical fiber. The process allows high sensitivity pressure sensors to be fabricated without incurring high splice losses. Simulations show large pressure sensitivities of up to 3.3 pm/bar are possible in 250 μm diameter fiber. We fabricated three dimensional

pressure sensors in both standard single-mode fiber and a large diameter fiber. Hydraulic pressure testing showed a pressure sensitivity of 0.41 pm/bar with a dynamic range of 300-600 bar. The fabrication technique has the potential to be used in a wide range of high performance fibers, including sapphire fiber for use in ultra-extreme environments.

Data Availability

The underlying data for Figs. 9, 10 and 11 are provided in Dataset 1 of the Supplementary Information [17]. For the purposes of open access, the authors have applied a Creative Commons Attribution (CC-BY) license to any Author Accepted Manuscript version.

Acknowledgement

The authors thank Clive Baker for his invaluable help with the hydraulic test setup and for providing some of the equipment.

References

[1] L. Albero Blanquer, F. Marchini, J. R. Seitz, N. Daher, F. Bétermier, J. Huang, C. Gervillié, and J.-M. Tarascon, "Optical sensors for operando stress monitoring in lithium-based batteries containing solid-state or liquid electrolytes," *Nature communications*, vol. 13, no. 1, pp. 1–14, 2022.

[2] Y. Zhao, Y. Zhu, M. Yuan, J. Wang, and S. Zhu, "A laser-based fiber bragg grating ultrasonic sensing system for structural health monitoring," *IEEE Photonics Technology Letters*, vol. 28, no. 22, pp. 2573–2576, 2016.

[3] T. Kao and H. Taylor, "High-sensitivity intrinsic fiber-optic fabry–perot pressure sensor," *Optics letters*, vol. 21, no. 8, pp. 615–617, 1996.

[4] C. M. Jewart, Q. Wang, J. Canning, D. Grobnic, S. J. Mihailov, and K. P. Chen, "Ultrafast femtosecond-laser-induced fiber bragg gratings in air-hole microstructured fibers for high-temperature pressure sensing," *Optics letters*, vol. 35, no. 9, pp. 1443–1445, 2010.

[5] T. Chen, Q. Wang, R. Chen, B. Zhang, C. Jewart, K. P. Chen, M. Maklad, and P. R. Swinehart, "Distributed high-temperature pressure sensing using air-hole microstructural fibers," *Optics letters*, vol. 37, no. 6, pp. 1064–1066, 2012.

[6] T. Chen, R. Chen, C. Jewart, B. Zhang, J. Canning, K. Cook, and K. P. Chen, "Thermally regenerated fiber bragg gratings in twin-air-hole microstructured fibers for high temperature pressure sensing," in *Fiber Optic Sensors and Applications VIII*, vol. 8028. SPIE, 2011, pp. 32–39.

[7] S. James, M. Dockney, and R. Tatam, "Simultaneous independent temperature and strain measurement using in-fibre bragg grating sensors," *Electronics Letters*, vol. 32, no. 12, pp. 1133–1134, 1996.

[8] P. Cavaleiro, F. Araujo, L. Ferreira, J. Santos, and F. Farahi, "Simultaneous measurement of strain and temperature using bragg gratings written in germanosilicate and boron-codoped germanosilicate fibers," *IEEE Photonics Technology Letters*, vol. 11, no. 12, pp. 1635–1637, 1999.

[9] J.-Y. Huang, J. Van Roosbroeck, J. Vlekken, A. B. Martinez, T. Geernaert, F. Berghmans, B. Van Hoe, E. Lindner, and C. Caucheteur, "Fbgs written in specialty fiber for high pressure/high temperature measurement," *Optics express*, vol. 25, no. 15, pp. 17 936–17 947, 2017.

[10] D. Goldstein, *Polarized Light*. CRC Press, 2017. [Online]. Available: https://books.google.co.uk/books?id=w6PMBQAAQBAJ

[11] P. S. Theocaris and E. E. Gdoutos, *Matrix theory of photoelasticity*. Springer, 2013, vol. 11.

[12] K. Zhou, M. Dubov, C. Mou, L. Zhang, V. K. Mezentsev, and I. Bennion, "Line-by-line fiber bragg grating made by femtosecond laser," *IEEE Photonics Technology Letters*, vol. 22, no. 16, pp. 1190–1192, 2010.

[13] S. Kiyama, S. Matsuo, S. Hashimoto, and Y. Morihira, "Examination of etching agent and etching mechanism on femotosecond laser microfabrication of channels inside vitreous silica substrates," *The Journal of Physical Chemistry C*, vol. 113, no. 27, pp. 11 560–11 566, 2009.

[14] L. Wong, T. Suratwala, M. Feit, P. Miller, and R. Steele, "The effect of hf/nh4f etching on the morphology of surface fractures on fused silica," *Journal of Non-Crystalline Solids*, vol. 355, no. 13, pp. 797–810, 2009.

[15] M. Wang, P. S. Salter, F. P. Payne, A. Shipley, S. M. Morris, M. J. Booth, and J. A. J. Fells, "Single-mode sapphire fiber bragg grating," *Optics Express*, vol. 30, no. 9, pp. 15 482–15 494, 2022.

[16] M. Kaiser, M. Kumkar, R. Leute, J. Schmauch, R. Priester, J. Kleiner, M. Jenne, D. Flamm, and F. Zimmermann, "Selective etching of ultrafast laser modified sapphire," in *Laser Applications in Microelectronic and Optoelectronic Manufacturing (LAMOM) XXIV*, vol. 10905. SPIE, 2019, pp. 19–30.

[17] T. Liu, Z. Song, R. J. Reeves, M. Wang, C. T. M. Doyle, M. J. Booth, and J. A. J. Fells, "Dataset 1 3d structured optical fiber pressure sensors," IEEE Dataport, doi 10.21227/4tpf-d753, 2024.